

Article

Phase Formation, Microstructure and Permeability of Fe-Deficient Ni-Cu-Zn Ferrites, (I): Effect of Sintering Temperature

Christoph Priese and Jörg Töpfer * 

Dept. SciTec., Ernst-Abbe-Hochschule Jena, 07745 Jena, Germany; christoph.priese@eah-jena.de

* Correspondence: Joerg.Toepfer@eah-jena.de; Tel.: +49-3641-205-479

Abstract: We have studied the densification, phase formation, microstructure, and permeability of stoichiometric and Fe-deficient Ni-Cu-Zn ferrites of composition $\text{Ni}_{0.30}\text{Cu}_{0.20}\text{Zn}_{0.50+z}\text{Fe}_{2-z}\text{O}_{4-(z/2)}$ with $0 \leq z \leq 0.06$ sintered at temperatures from 900 °C to 1150 °C. The shrinkage is shifted from 1000 °C for $z = 0$ towards lower temperatures and reaches its maximum rate at 900 °C for $z = 0.02$. Stoichiometric ferrites show regular growth of single-phase ferrite grains if sintered at $T_s \leq 1100$ °C. Sintering at 1150 °C leads to the formation of a small amount of Cu_2O , triggering exaggerated grain growth. Fe-deficient compositions ($z > 0$) form Cu-poor stoichiometric ferrites coexisting with a minority CuO phase after sintering at 900–1000 °C. At $T_s \geq 1050$ °C, CuO transforms into Cu_2O , and exaggerated grain growth is observed. The formation of Cu oxide second phases is investigated using XRD, SEM, and EDX. The permeability of the ferrites increases with sintering temperature up to a maximum permeability of $\mu = 230$ for $z = 0$ or $\mu = 580$ for $z = 0.02$, respectively, at $T_s = 1000$ °C. At higher sintering temperatures, the permeability decreases, which is due to the formation of a microstructure with intra-crystalline porosity in large grains, and a non-magnetic Cu oxide grain boundary phase.



Citation: Priese, C.; Töpfer, J. Phase Formation, Microstructure and Permeability of Fe-Deficient Ni-Cu-Zn Ferrites, (I): Effect of Sintering Temperature.

Magnetochemistry **2021**, *7*, 118.

<https://doi.org/10.3390/magnetochemistry7080118>

Academic Editor: Vasiliki Tsakaloudi

Received: 5 July 2021

Accepted: 9 August 2021

Published: 14 August 2021

Publisher's Note: MDPI stays neutral with regard to jurisdictional claims in published maps and institutional affiliations.



Copyright: © 2021 by the authors. Licensee MDPI, Basel, Switzerland. This article is an open access article distributed under the terms and conditions of the Creative Commons Attribution (CC BY) license (<https://creativecommons.org/licenses/by/4.0/>).

Keywords: soft ferrites; magnetic permeability; polycrystalline microstructure

1. Introduction

Ni-Cu-Zn ferrites are an important group of soft magnetic materials for many applications including power ferrites, EMI devices, and multilayer inductors. The main advantages of Ni-Cu-Zn ferrites are their low sintering temperature T_s , high resistivity, medium permeability, low loss, and good performance up to MHz frequencies [1–4]. Magnetic properties critically depend, among other factors, on ferrite composition and microstructure. Owing to the lower sintering temperatures of Ni-Cu-Zn ferrites as compared with Ni-Zn or Mn-Zn ferrites, it is necessary to investigate in detail the effect of sintering conditions on the microstructure and magnetic properties of the ferrites, and to design specific sintering protocols to achieve optimum performance. Many studies were performed to investigate the low-temperature sintering behavior of Ni-Cu-Zn ferrites. For applications in multilayer inductors, ferrites are cofired with silver metallization as low as $T_s \leq 900$ °C. Most studies report on a specific ferrite composition, which is fired at 900 °C using a sintering additive, as well as its microstructure formation, permeability, and DC bias superposition behavior [5–8]. Papers reporting correlations between Ni-Cu-Zn ferrite composition, sintering behavior, and magnetic properties, on the other hand, are scarce [9,10]. A common feature of low-firing ferrite compositions is a small deficiency of iron oxide in the starting oxide mixture (<50 mol% Fe_2O_3). Such Fe-deficient compositions typically translate into a spinel formula with less than two Fe per formula unit, for example, $\text{Me}_{1.02}\text{Fe}_{1.98}\text{O}_{3.99}$, as compared with stoichiometric ferrites with 50 mol% Fe_2O_3 and the formula unit MeFe_2O_4 . It has been reported that Fe-deficiency enhances densification [11–14]. Moreover, it has been found that secondary phases might precipitate at grain boundaries and affect the magnetic properties. In Fe-deficient ferrites, tenorite CuO was found to form at triple points or grain boundaries

after sintering at 900 °C [14] and at 1100 °C [15]. The formation of microstructural defects including precipitates of copper at grain boundaries was also observed in Fe-deficient Ni-Cu-Zn ferrites using TEM [16]. On the other hand, Sun et al. reported the formation of ZnO as secondary phase in Fe-deficient samples [17]. For a stoichiometric Ni-Cu-Zn ferrite, a detailed study of phase composition and microstructure revealed precipitation of CuO and ZnO after sintering at 1200 °C, with their concentrations depending on green density, sintering temperature, and cooling rate [18,19]. Nazrin et al. [20] did not detect any secondary phases in Fe-deficient ferrites.

In this contribution, we report a systematic study on phase formation, microstructure, and permeability of Fe-deficient $\text{Ni}_{0.30}\text{Cu}_{0.20}\text{Zn}_{0.50+z}\text{Fe}_{2-z}\text{O}_{4-(z/2)}$ ferrites with $0 \leq z \leq 0.06$. In part I of this study, we focus on the effect of sintering temperature in air atmosphere. In part II, we will describe in detail the effect of oxygen partial pressure. It is found that the grain size increases with sintering temperature T_s until a critical temperature, where intra-crystalline pores and abnormally grown large grains start to appear. For $z \geq 0$, CuO precipitates at grain boundaries, which is transformed into Cu_2O at high temperature. The amount of CuO increases with Fe-deficiency z . The permeability increases with T_s and grain size in the range of predominance of regular grain growth. At higher T_s , the formation of Cu_2O at grain boundaries initiates abnormal grain growth and intra-crystalline porosity and, consequently, a decrease in permeability is observed.

2. Results

2.1. Powder Properties

Single-phase ferrite powders were obtained after calcination at 900 °C (XRD results not shown here). After milling, a mean particle size of the powder of $d_{50} = 0.7 \mu\text{m}$ was measured using laser diffraction, which represents the size of aggregates. The specific surface of the ferrite powder of $S = 5 \text{ m}^2/\text{g}$ corresponds to a mean particle diameter of primary particles of $d_{\text{BET}} = 220 \text{ nm}$.

2.2. Shrinkage and Densification Behavior

Dilatometric shrinkage measurements of pellets made from milled powders demonstrate that the Fe-deficiency z significantly affects the shrinkage and shrinkage rate in $\text{Ni}_{0.30}\text{Cu}_{0.20}\text{Zn}_{0.50+z}\text{Fe}_{2-z}\text{O}_{4-(z/2)}$ (Figure 1a).

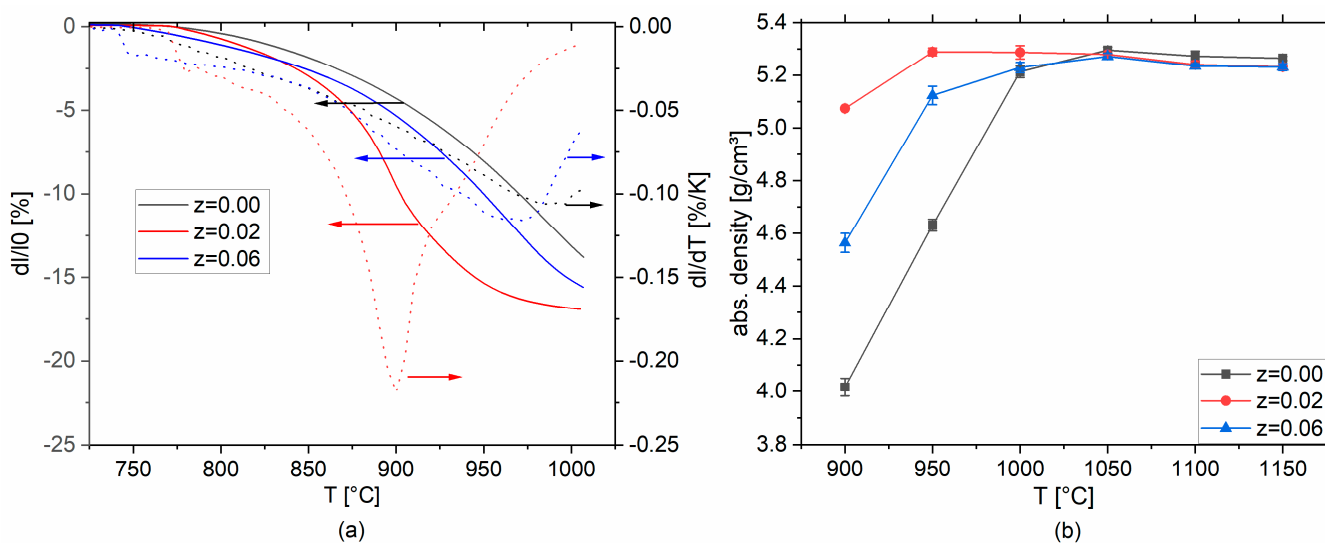


Figure 1. (a) Relative shrinkage and shrinkage rate vs. temperature and (b) absolute density vs. sintering temperature for $0 \leq z \leq 0.06$.

Stoichiometric $\text{Ni}_{0.3}\text{Cu}_{0.2}\text{Zn}_{0.5}\text{Fe}_2\text{O}_4$ ($z = 0$) has its maximum shrinkage rate at about 970 °C. Shrinkage is shifted towards lower temperatures with increasing Fe-deficiency;

for $z = 0.02$, the maximum shrinkage is at $900\text{ }^{\circ}\text{C}$. For $z > 0.02$, the temperature of the maximum shrinkage rate is increased (Figure 1a). The observed differences in the shrinkage of stoichiometric and Fe-deficient Ni-Cu-Zn ferrites are also reflected in the densification behavior. Stoichiometric Ni-Cu-Zn ferrite ($z = 0$) experiences limited densification at $900\text{ }^{\circ}\text{C}$ (75%) and sintering at $T_s \geq 1000\text{ }^{\circ}\text{C}$ is required for densification (Figure 1b). Ferrites with $z = 0.02$ exhibit excellent densification behavior and sintering at $900\text{ }^{\circ}\text{C}$ already leads to good density of $5.07(1)\text{ g/cm}^3$ (95%); sintering at $T \geq 950\text{ }^{\circ}\text{C}$ results in almost complete densification of $5.28(1)\text{ g/cm}^3$ (99%). For larger Fe-deficiency ($z = 0.06$), a somewhat reduced densification is observed and a sintering temperature of $T_s = 1000\text{ }^{\circ}\text{C}$ is necessary to achieve good densities.

2.3. Microstructure and Element Distribution

SEM micrographs of samples with different values of Fe-deficiency z sintered at temperatures between $900\text{ }^{\circ}\text{C}$ and $1150\text{ }^{\circ}\text{C}$ are presented in Figure 2. The stoichiometric ferrite ($z = 0.00$) exhibits regular grain growth up to $T_s \leq 1100\text{ }^{\circ}\text{C}$, whereas a sample sintered at $1150\text{ }^{\circ}\text{C}$ consists of very large grains of about 1 mm in size as a result of exaggerated grain growth. For samples sintered at $T_s \geq 1050\text{ }^{\circ}\text{C}$, intra-crystalline porosity is observed.

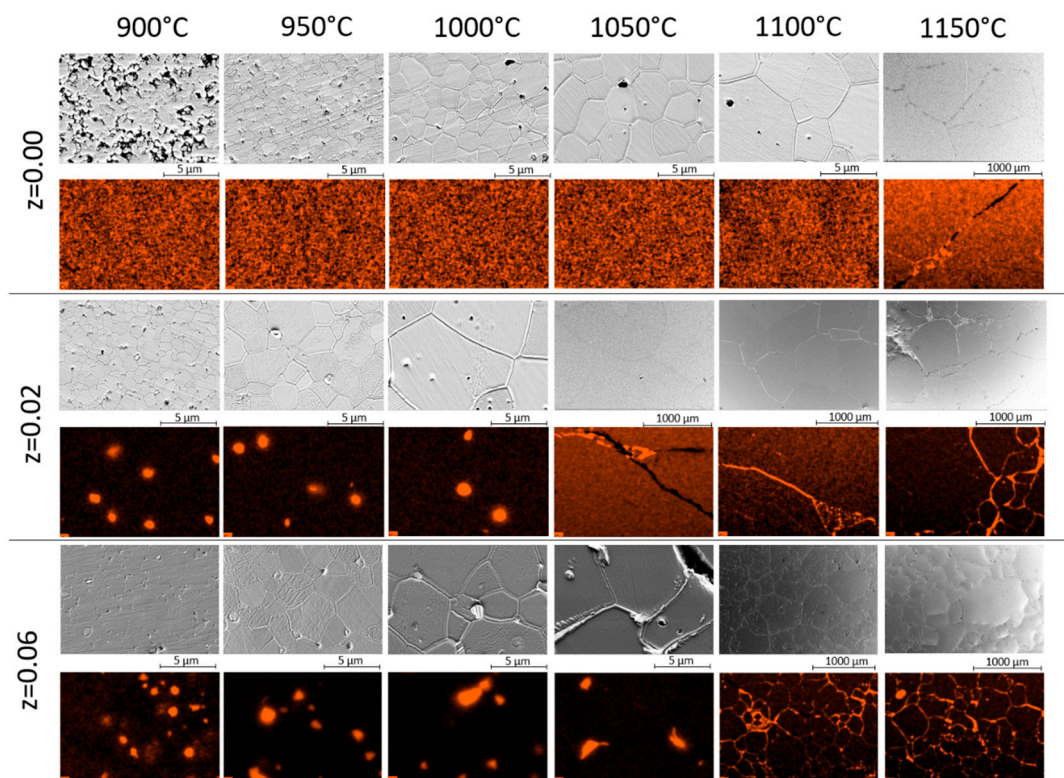


Figure 2. Microstructure images (SEM, SE mode) and EDX mapping of Cu-distribution in dependence of sintering temperature for $z = 0.00, 0.02$, and 0.06 (representative examples; SEM and EDX not from the same sample area).

The evolution of grain size versus temperature (Figure 3) confirms regular grain growth behavior for $T_s < 1150\text{ }^{\circ}\text{C}$.

For Fe-deficient ferrites ($z > 0$), exaggerated grain growth already starts to appear at lower temperatures, at $T_s > 1000\text{ }^{\circ}\text{C}$ for $z = 0.02$ and at $T_s > 1050\text{ }^{\circ}\text{C}$ for $z = 0.06$ (Figures 2 and 3). Pores within the ferrite grains were found at $T_s = 1000\text{ }^{\circ}\text{C}$ for $z = 0.02$ and at $T_s = 1050\text{ }^{\circ}\text{C}$ for $z = 0.06$, i.e., at temperatures about $50\text{ }^{\circ}\text{C}$ below the beginning of exaggerated grain growth.

The composition of the matrix grains and grain boundary regions was studied using energy dispersive X-ray analysis (EDX). The composition of the ferrite matrix grains

remains unchanged (within the given resolution) for different sintering temperatures, as demonstrated for $z = 0.02$ in Figure 4a.

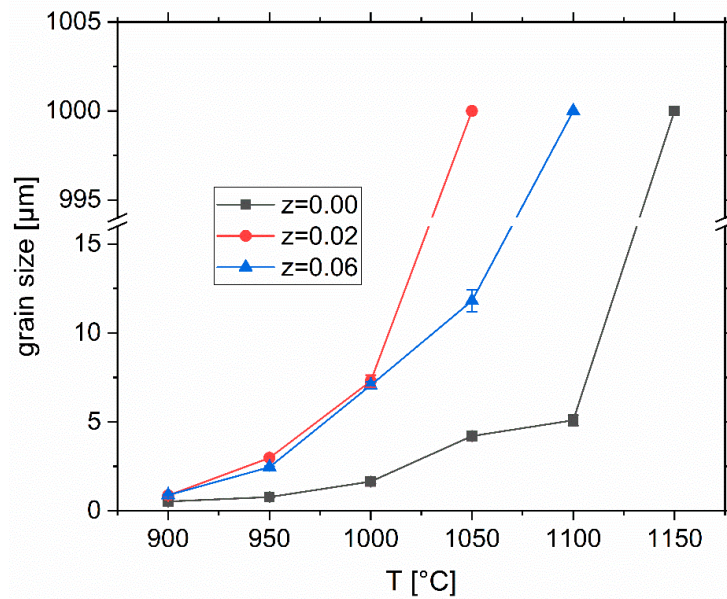


Figure 3. Ferrite grain size vs. sintering temperature for $0 \leq z \leq 0.06$.

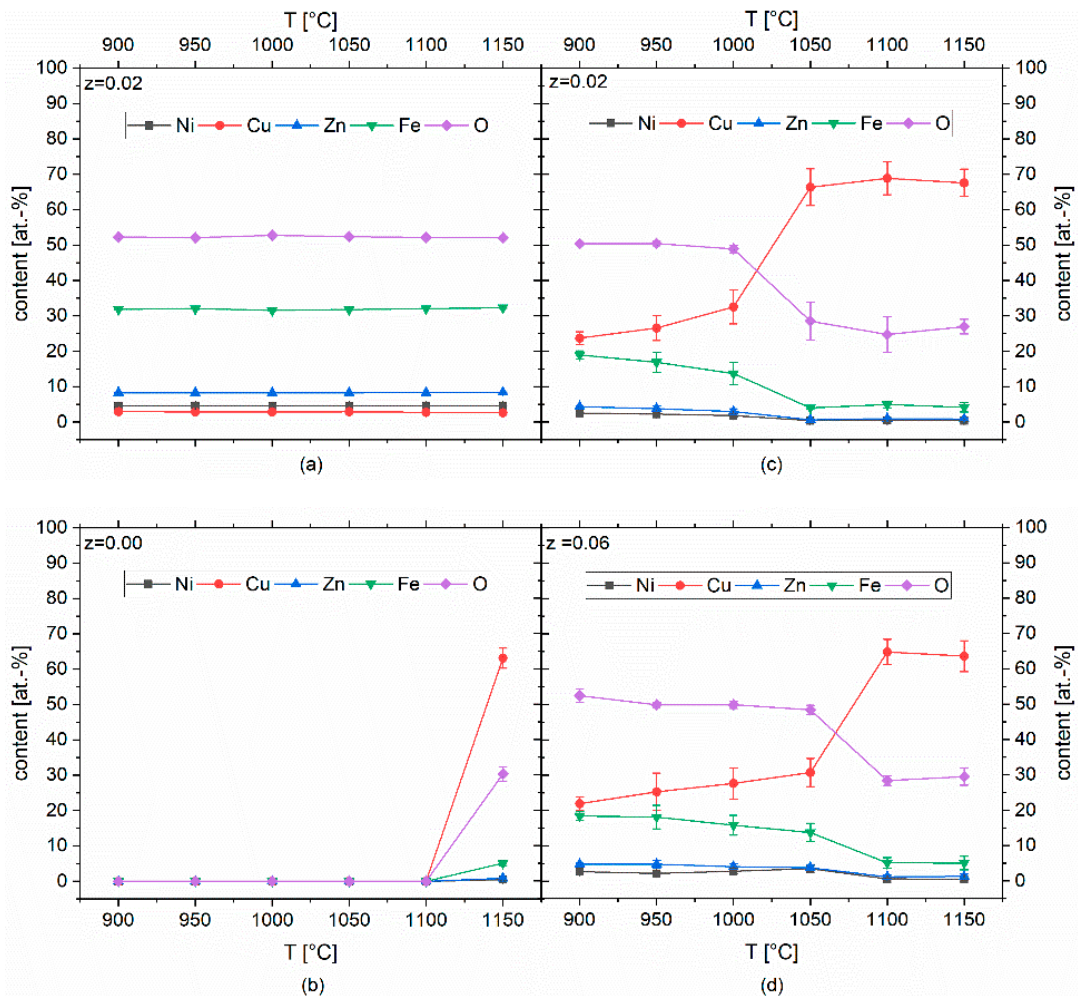


Figure 4. Chemical composition determined using EDX point scans vs. sintering temperature of (a) ferrite matrix grains ($z = 0.02$) and triple points or grain boundary regions for (b) $z = 0.00$, (c) $z = 0.02$, and (d) $z = 0.06$.

The distribution of the copper oxide phase in the microstructure was studied in some detail. In addition to SEM micrographs, Figure 2 shows EDX mappings of the Cu distribution for all samples and sintering temperatures T_s . In the case of stoichiometric ferrites ($z = 0$), a homogeneous distribution of Cu is found, except for the sample sintered at 1150 °C, where enrichment of Cu is detected at grain boundaries between very large grains.

For Fe-deficient ferrites ($z = 0.02$ and 0.06), Cu-rich regions in the triple points between regularly grown ferrite grains are found. A different situation is observed in microstructures dominated by accelerated grain growth. At $T_s \geq 1050$ °C for $z = 0.02$ and at $T_s \geq 1100$ °C for $z = 0.06$, the Cu oxide phase is found to form a network along the grain boundaries of the very large ferrite grains (Figure 2). The variation of the elemental concentrations of copper and oxygen from EDX measurements is depicted versus sintering temperature in Figure 4b–d. For $z = 0$, a separate copper oxide phase with 63.1 at% Cu and 30.3 at% oxygen is detected at 1150 °C (Figure 4b). For Fe-deficient spinel ferrites, Cu-, Fe-, and O-contents of about 30 at%, 15 at%, and 50 at%, respectively, were found at low T_s . At higher sintering temperatures of $T_s \geq 1050$ °C for $z = 0.02$ and at $T_s \geq 1100$ °C for $z = 0.06$, different elemental concentrations of about 66 at% Cu, minor quantities of iron, and 30 at% O are observed (Figure 4c,d). This indicates a phase transition from tenorite CuO (theor. 50 at% Cu and O) to cuprite Cu₂O (theor. 66 at% Cu and 33 at% O) to take place at around 1050 °C in the Cu-oxide grain boundary phase.

2.4. Phase Formation

The phase composition of the ferrites was also investigated using X-ray diffraction (XRD). A single-phase ferrite with spinel-type structure was found at $z = 0$ (not shown here). In the XRD pattern of the sample with $z = 0.06$ (Figure 5), an additional peak at $2\theta = 38.7^\circ$, which is identified as (110) reflection of tenorite CuO, appears for samples sintered between 900 °C and 1100 °C.

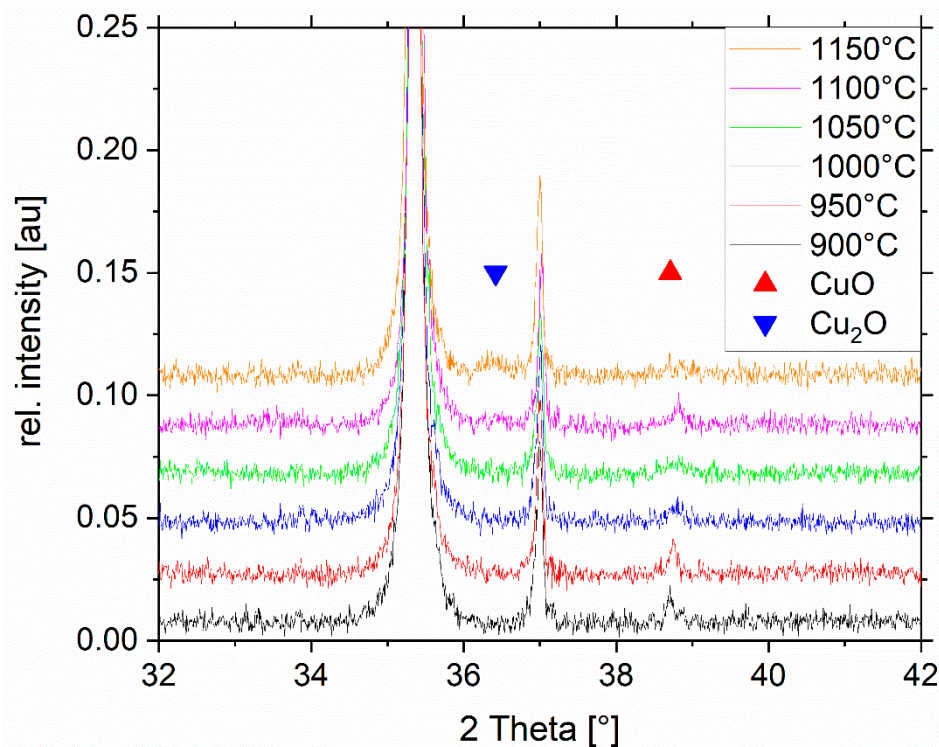


Figure 5. XRD patterns of $z = 0.06$ sintered at temperatures of 900–1150 °C.

This peak was hardly detectable in the ferrite with $z = 0.02$, because, in that case, the CuO concentration seems to be below the XRD detection limit. For a sample with $z = 0.06$ sintered at 1150 °C, this CuO peak disappears and another one at about $2\theta = 36.4^\circ$ is found, which confirms a phase transition into cuprite Cu₂O (Figure 5). The cubic lattice

parameters a_0 of the spinel ferrites with $z = 0, 0.02$, and 0.06 are plotted versus sintering temperature in Figure 6a. An increase of a_0 with z reflects a change in the ferrite matrix grain compositions. Moreover, a_0 also increases somewhat with T_s (for each Fe-deficiency z), indicating a very small change in ferrite composition.

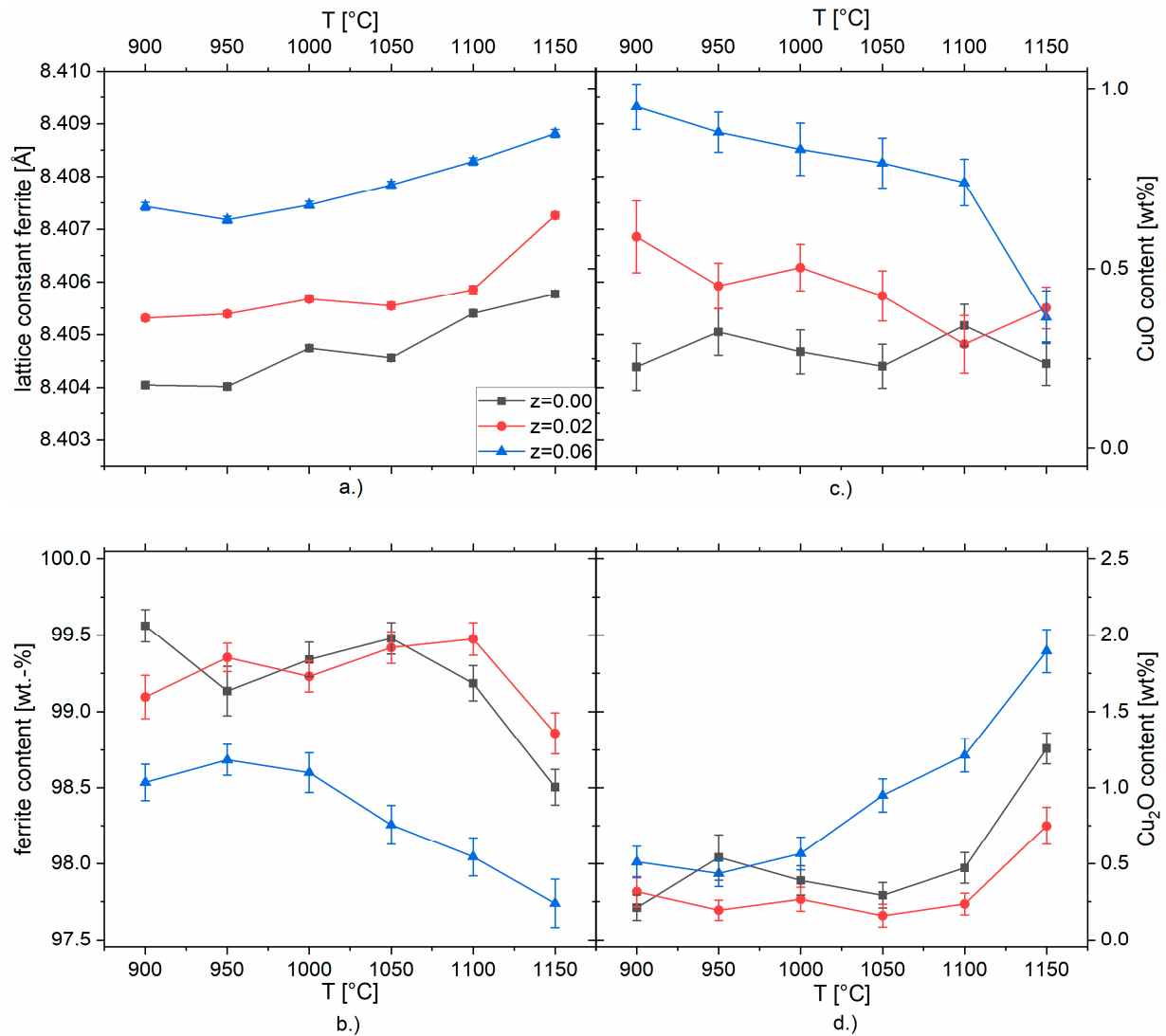


Figure 6. (a) Lattice parameters a_0 , (b) ferrite content, (c) CuO content, and (d) Cu₂O content from Rietveld refinements for $0 \leq z \leq 0.06$ vs. sintering temperature.

The phase compositions of the samples were obtained from Rietveld refinements of XRD powder data. The concentrations of ferrite, tenorite CuO, and cuprite Cu₂O are shown as a function of sintering temperature T_s in Figure 6b–d. For $z = 0$, the ferrite concentration is >99 wt%, except for the sample sintered at 1150 °C, with slightly reduced ferrite content of about 98.5 wt%. Correspondingly, the CuO content (<0.25 wt%) and the Cu₂O contents are negligibly small (<0.5 wt%) for $T_s = 900$ °C to 1100 °C, but the concentration of Cu₂O increases to 1.25 wt% at 1150 °C (Figure 6d). For $z = 0.02$, the ferrite content is also >99 wt%, except for $T_s = 1150$ °C, where the ferrite content is 98.7 wt%. The CuO content is about 0.5 wt% (Figure 6c). The Cu₂O content is negligibly small at $T_s \leq 1100$ °C, but increases to 0.8 wt.% at $T_s = 1150$ °C (Figure 6d). For larger Fe-deficiency of $z = 0.06$, a clearer situation is observed: the ferrite content (Figure 6b) slightly decreases from 98.5 wt% at $T_s = 900$ °C to 97.7 wt.% at $T_s = 1150$ °C. The CuO concentration (Figure 6c) slightly decreases as well from about 0.9 wt% at $T_s = 900$ °C to 0.7 wt% at $T_s = 1100$ °C, and then steeply declines

to 0.35 wt% at $T_s = 1150$ °C. Simultaneously, the cuprite Cu_2O concentration (Figure 6d) increases with T_s , reaching a maximum of almost 2 wt% at $T_s = 1150$ °C.

2.5. Thermal Analysis

Thermoanalytical investigations were carried out to characterize the phase transformation behavior (Figure 7). Thermogravimetry (TG) curves of Fe-deficient ferrites with $z = 0.02$ and 0.06 exhibit a slight mass loss at about 1040 °C, indicating a reduction of the CuO secondary phase and formation of Cu_2O . The stoichiometric ferrite ($z = 0$) does not show such mass loss in that temperature range, but a small mass loss at 1135 °C, which might signal ferrite decomposition and Cu_2O formation. For comparison, pure CuO powder shows a mass loss starting at 1030 °C, indicating reduction and release of oxygen.

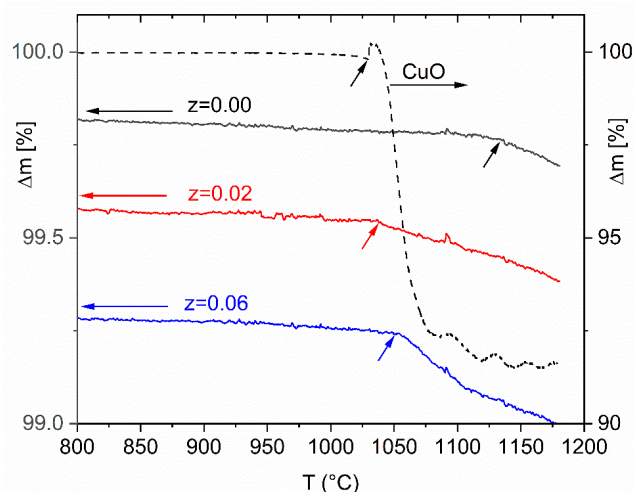


Figure 7. Relative mass losses (TG) for $z = 0.00$, $z = 0.02$, $z = 0.06$, and CuO vs. temperature.

2.6. Magnetic Permeability

The complex permeability spectra of two representative samples are shown in Figure 8. A ferrite with $z = 0.06$ sintered at 950 °C (Figure 8a) with a homogeneous fine-grained microstructure and grain size of $g = 2.5(1)$ μm shows a permeability of $\mu' = 386$ at 1 MHz. The imaginary part of permeability μ'' has a broad peak centered at 10 MHz. A sample of the same composition sintered at 1100 °C with very large grains has a $\mu' = 300$ at 1 MHz, in combination with a flat and very broad μ'' signal (Figure 8b).

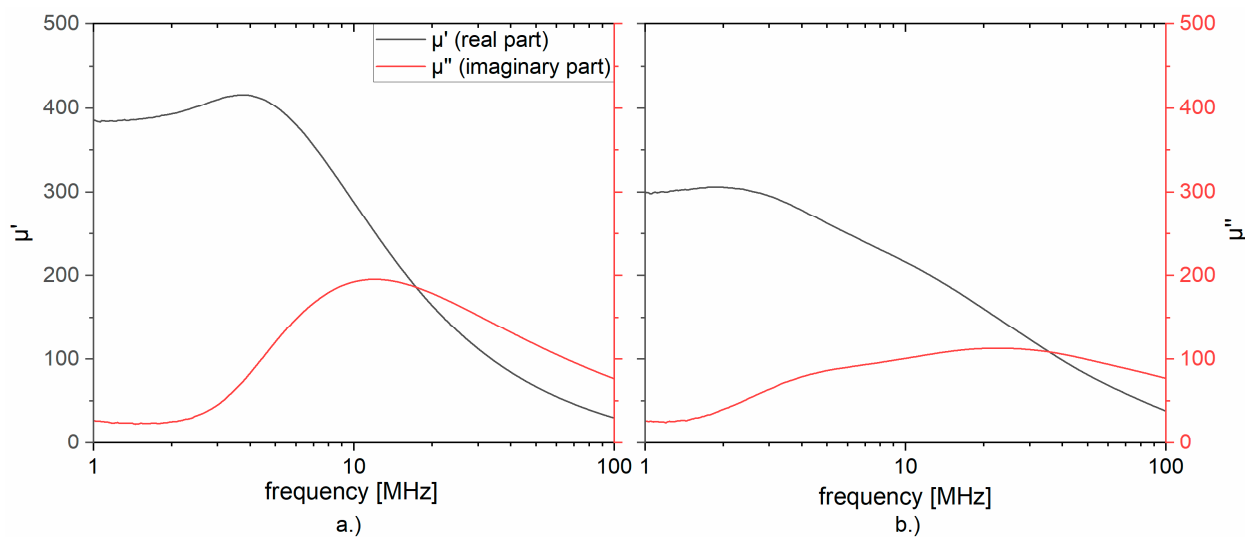


Figure 8. Permeability spectra vs. frequency for (a) $z = 0.06$ sintered at 950 °C with fine-grained microstructure and (b) $z = 0.06$ sintered at 1100 °C with large grains.

The variation of permeability versus sintering temperature is shown in Figure 9 for all samples. Stoichiometric ferrites ($z = 0$) have the lowest permeability values and the Fe-deficient samples with $z = 0.02$ show large permeability up to $T_s = 1000$ °C. All three samples series, however, exhibit the same general behavior with a maximum permeability at an intermediate sintering temperature and the permeability decreasing at higher sintering temperatures. This maximum permeability appears at $T_s = 1000$ °C for $z = 0$ ($\mu = 247$) and $z = 0.02$ ($\mu = 594$), whereas at $z = 0.06$, a maximum $\mu = 437$ is found at $T_s = 1050$ °C. The variation of permeability versus grain size shows a similar picture (Figure 9b). The permeability increases with grain size and decreasing inter-crystalline porosity (increasing density) for homogeneous fine-grained microstructures, levels out, and goes through a maximum value of permeability, and finally decreases for samples with microstructures with intra-crystalline porosity and large grains formed by discontinuous grain growth.

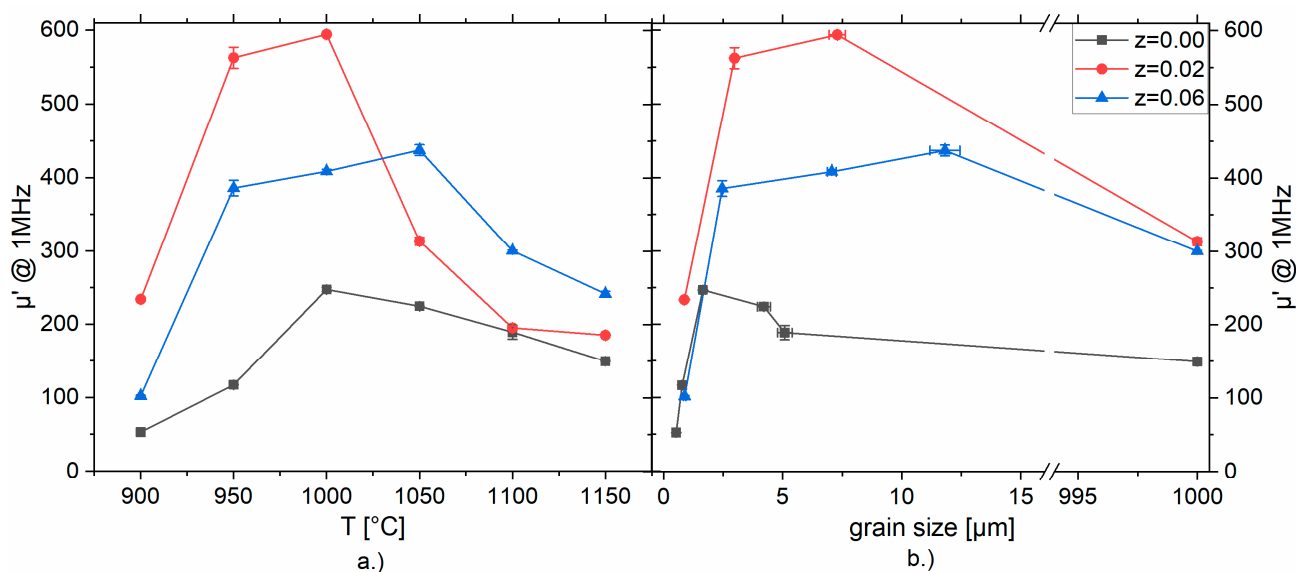
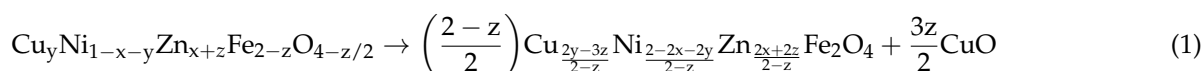


Figure 9. Permeability @ 1MHz (a) vs. sintering temperature and (b) vs. grain size of ferrites with $0 \leq z \leq 0.06$.

3. Discussion

The densification, microstructure, phase composition, and magnetic properties of stoichiometric and Fe-deficient Ni-Cu-Zn ferrites exhibit significant differences. This is documented here for the ferrite series $\text{Ni}_{0.30}\text{Cu}_{0.20}\text{Zn}_{0.50+z}\text{Fe}_{2-z}\text{O}_{4-(z/2)}$ with Fe-deficiency $0 \leq z \leq 0.06$. An important advantage of a small Fe-deficiency ($z = 0.02$) is an enhanced sinter-ability, enabling co-firing with silver metallization at 900 °C (Figure 1). In a previous study, we have reported similar Fe-deficient Ni-Cu-Zn ferrites sintered at 900 °C [14]. We observed CuO as a second phase after sintering at 900 °C and concluded that the nominally Fe-deficient (sub-stoichiometric) compositions consist of mixture of a Cu-poor stoichiometric ferrite main phase and CuO as the secondary phase [14]:



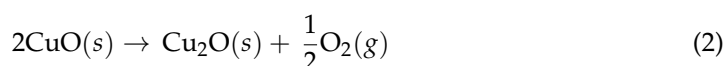
For ferrite compositions reported here ($y = 0.20$ and $x = 0.50$), Equation (1) results in the formation of a spinel $\text{Cu}_{0.17}\text{Ni}_{0.30}\text{Zn}_{0.53}\text{Fe}_2\text{O}_4$ and 0.03 CuO for an Fe-deficiency of $z = 0.02$, whereas for $z = 0.06$, the ferrite $\text{Cu}_{0.11}\text{Ni}_{0.31}\text{Zn}_{0.58}\text{Fe}_2\text{O}_4$ coexists with 0.09 CuO. The existence of tenorite CuO is likely to be the reason for the observed shift of shrinkage towards lower temperature (Figure 1a) and the increased density of Fe-deficient ferrites at sintering temperatures between 900 and 1000 °C (Figure 1b).

In this study, we have extended the range of sintering temperatures. For Fe-deficient ferrites, we observed the coexistence of copper oxide phases for all sintering temperatures.

This finding is in contrast to the results of other studies: Ni-Cu-Zn ferrites with iron-deficiency between 47 and 50 mol% Fe₂O₃ (sintered between 1040 and 1200 °C) were reported to contain a ZnO secondary phase [17]. Barba et al. reported a very detailed study on the microstructure and formation of ZnO and CuO secondary phases in stoichiometric samples of Cu_{0.12}Ni_{0.23}Zn_{0.65}Fe₂O₄ sintered at 1200 °C and rapidly cooled (quenched or 20 K/min cooling rate) [18] or sintered at temperatures between 1000 °C and 1200 °C [19] (cooling rate 20 K/min). With a cooling rate of 5 K/min used in this study, we did not observe any ZnO formation in our samples.

Stoichiometric Ni-Cu-Zn ferrite ($z = 0$) exhibits a homogeneous microstructure, as demonstrated by SEM and EDX (Figure 2), with regular grain growth up to $T_s = 1100$ °C (Figure 3), and a single ferrite phase as confirmed by XRD (Figure 6). However, the sample $z = 0$ sintered at 1150 °C shows the formation of large grains of about 1000 µm in size with the precipitation of some Cu oxide at the grain boundaries (Figure 2), which was identified as Cu₂O using EDX (Figure 4b). Rietveld refinement of XRD data confirmed the formation of a small, but significant concentration of cuprite Cu₂O (Figure 6d). Another important feature is the appearance of intra-crystalline porosity in stoichiometric samples sintered at $T_s = 1050$ °C and 1100 °C (Figure 2). For Fe-deficient ferrites with $z = 0.02$ and $z = 0.06$ homogeneous microstructures with regular grain growth are found up to sintering temperatures of 1000 °C and 1050 °C, respectively (Figure 2). Simultaneously, EDX Cu distribution mappings reflect the formation of Cu-enriched regions at triple points between the ferrite grains. Quantitative EDX analysis revealed the Cu-oxide at the triple points to be tenorite CuO (Figure 4c,d) with about 24–33 at% Cu, 18–13 at% Fe, and about 50 at% oxygen for $z = 0.02$ sintered from 900 °C to 1000 °C (Figure 4c) and, similarly, with about 24–30 at% Cu, 18–13 at% Fe, and about 50 at% oxygen for $z = 0.06$ sintered from $T_s = 900$ °C to 1050 °C (Figure 4d). The measured Fe content in the triple point regions might be an artefact of EDX analysis, as part of the measured Fe X-ray intensity might be emitted from surrounding ferrite grains (although the triple point areas are larger than 1–2 µm in diameter). Another interpretation of the simultaneous presence of Fe besides Cu in triple points is a possible dissolution of iron in the tenorite lattice; the synthesis and properties of Fe_xCu_{1-x}O nanoparticles with $x \leq 0.3$ [21] or $x \leq 0.125$ [22] were reported recently.

The coexistence of Cu oxides and ferrites grains was confirmed using XRD (Figure 5). For Fe-deficient samples with $z = 0.06$ a temperature-dependent phase transition of the Cu oxide secondary phase from tenorite CuO to cuprite Cu₂O was confirmed. No indication of zincite ZnO segregation was found, as discussed above. The slight increase of the cubic ferrite spinel lattice parameter a_0 versus z (Figure 6a) points to a small change in the ferrite composition with z (see Equation (1) as discussed above). As increasing z implies an increase of Zn content in the ferrite main phase, the observed variation of a_0 with z is consistent with the similar trend reported for Ni-Zn ferrites [23]. The results of quantitative Rietveld refinements of the phase compositions shed more light on the variation of the chemistry of the Cu oxide secondary phase with temperature and z . Whereas the stoichiometric ferrites ($z = 0$) have no tenorite secondary phase, the CuO-concentration increases from about 0.5 wt% for $z = 0.02$ to 0.9 wt% for $z = 0.06$ in the Fe-deficient ferrites (Figure 6c). At higher sintering temperatures, cuprite Cu₂O is present, with a maximum content of 1.9 wt% at $T_s = 1150$ °C for $z = 0.06$ (Figure 6d). The Cu oxide phase present at triple points and grain boundaries undergoes a phase transformation:



at $T_s > 1050$ °C. This is confirmed by thermal analysis (Figure 7). Thermal decomposition of tenorite CuO starts at 1030 °C in air. Small mass losses were observed at 1040 °C and 1050 °C in the Fe-deficient ferrites with $z = 0.02$ and 0.06, respectively, (Figure 7), indicating a reduction of the tenorite second phase. With increasing temperature, the remaining CuO coexists with Cu₂O and forms a eutectic at 1080 °C [24], triggering changes in grain growth behavior owing to the presence of a liquid phase.

The variation of the phase and microstructure formation in Fe-deficient Ni-Cu-Zn ferrites as a function of sintering temperature may be summarized in three consecutive regions:

- (I) The ferrites exhibit normal grain growth. Some remaining inter-crystalline porosity is reduced with increasing T_s . The stoichiometric ferrite ($z = 0$) is single-phase spinel, and the Fe-deficient samples ($z > 0$) contain a small amount of tenorite CuO evenly distributed at the triple points between ferrite grains.
- (II) At a critical temperature, for example, at $T_s = 1050$ °C for $z = 0$, $T_s = 1000$ °C for $z = 0.02$, and $T_s = 1050$ °C for $z = 0.06$, intra-crystalline porosity starts to appear within the ferrite grains. Regular grain growth still dominates.
- (III) At a higher sintering temperature, i.e., at $T_s = 1150$ °C for $z = 0$, $T_s = 1050$ °C for $z = 0.02$, and $T_s = 1100$ °C for $z = 0.06$, a CuO/Cu₂O liquid phase appears, forming a network along the grain boundaries and triggering exaggerated growth of the ferrite grains.

The permeability spectra of the ferrites $\text{Ni}_{0.30}\text{Cu}_{0.20}\text{Zn}_{0.50+z}\text{Fe}_{2-z}\text{O}_{4-(z/2)}$ ($0 \leq z \leq 0.06$) reflect the different microstructures of the samples. As an example, a ferrite with $z = 0.06$ sintered at 950 °C and 1100 °C shows fine-grained homogeneous or large-grained microstructures, respectively (Figure 2). The permeability of the sample sintered at 950 °C (Figure 8a) is $\mu' = 390$ (1 MHz) and starts to decay at 4 MHz with a maximum of μ'' at 10 MHz. The ferrite sintered at 1100 °C (Figure 8b) with large grains and porosity within the grains exhibits a reduced permeability of $\mu' = 300$ (1 MHz) with a gradual decay over the whole frequency spectrum and a corresponding broad μ'' peak with its maximum at 30 MHz. This is expected because, according to Snoek's law, the shift of the resonance frequency toward higher frequencies is accompanied by a decrease of the absolute values of the permeability.

The intra-crystalline pores in the sample sintered at 1100 °C act as pinning centers for domains and impede domain wall displacement, and thus reduce the permeability. A similar comparison of two Ni-Cu-Zn ferrites with the same chemistry, but different microstructure was reported by Su et al. [25].

The variation of permeability (at 1 MHz) for stoichiometric ($z = 0$) and Fe-deficient ($z > 0$) ferrites versus sintering temperature displays a characteristic behavior: the permeability increases at lower sintering temperatures, goes through a maximum, and decreases at high sintering temperatures (Figure 9a). A similar variation of microstructures and permeability with sintering temperature was described for $\text{Ni}_{0.32}\text{Cu}_{0.10}\text{Zn}_{0.58}\text{Fe}_2\text{O}_4$ by Su et al. [26], and the observed permeability curve of this stoichiometric ferrite was interpreted based on different contributions from domain wall motion and spin rotation magnetization processes. However, as demonstrated in this study, in the case of Fe-deficient Ni-Cu-Zn ferrites, the secondary phase formation and the corresponding microstructures are considered as major factors controlling the permeability of the samples. In region (I) in Fe-deficient ferrites with homogeneous microstructures and small CuO concentrations, the sample density and grain size increase with T_s . Consequently, an increase of permeability is observed as well (Figure 9a). In region (II), intra-crystalline pores tend to hinder domain wall motion and initiate a decrease in permeability. In region (III), however, exaggerate growth of grains with intra-crystalline pores due to the appearance of a liquid phase at high T_s as well as the appearance of a solidified non-magnetic Cu-oxide layer at the grain boundaries during cooling are major factors leading to a continuous reduction of permeability. The increase of permeability of Fe-deficient ferrites as compared with the stoichiometric ferrite at $T_s \leq 1000$ °C is due to higher density; the reduced porosity for $z = 0.02$ enhances domain wall mobility and permeability. For $z > 0.02$, on the other hand, the higher amount of segregated, non-magnetic Cu oxide at triple points and grain boundaries tends to reduce the permeability.

Finally, we discuss the variation of permeability with grain size. The following characteristic features are observed (Figure 9b): the permeability increases with grain size up to a maximum permeability followed by a significant decrease of permeability, which is coupled to the appearance of large grains of about 1 mm in size separated by grain

boundaries formed by a solidified Cu oxide phase. The increase of permeability with grain size in the range of regular grain growth (region I) and levelling of permeability in region (II) is consistent with the non-magnetic grain boundary model [27] assuming the ferrite grains to be surrounded by a non-magnetic grain boundary layer of thickness δ . The effective permeability μ_e scales with the grain size G as follows:

$$\mu_e = \frac{\mu_i \cdot G}{\mu_i \cdot \delta + G} \quad (3)$$

with μ_i as permeability of the grain interior. For Fe-deficient Ni-Cu-Zn ferrites ($z = 0.02$ and 0.06), the formation of non-magnetic tenorite CuO between ferrite grains promotes densification and grain growth and boosts the permeability in region (I). In region (II), intra-crystalline pores act as domain pinning centers and start to reduce the permeability. Finally, liquid-phase sintered samples with pores in large grains and Cu-oxide layers as grain boundary networks exhibit smaller permeabilities (region III).

4. Materials and Methods

Ferrite powders of composition $\text{Ni}_{0.30}\text{Cu}_{0.20}\text{Zn}_{0.50+z}\text{Fe}_{2-z}\text{O}_{4-(z/2)}$ with $0 \leq z \leq 0.06$ were prepared by the standard ceramic route. $\alpha\text{-Fe}_2\text{O}_3$ (Voest Alpine, Linz, Austria, HPG80); NiO (Inco, Black Nickel Oxide, Grade F), CuO (Alpha Aesar, Karlsruhe, Germany), and ZnO (Harzsiegel, Heubach, Germany, standard grade) were used as starting materials. The oxides were wet mixed for 12 h in a polyethylene container. After drying, the powder was calcined at 900 °C for 2 h, and subsequently milled in a planetary ball mill (Fritsch Pulverisette 7; Idar-Oberstein, Germany) in POM grinding beakers for 4 h (170 rpm) using zirconia grinding media (diameter 1 mm). The powders were compacted using polyvinyl alcohol as a binder to produce pellets for sintering studies or toroids for permeability measurements. The samples were sintered for 4 h at temperatures between 900 °C and 1150 °C in air (heating/cooling rate of 5 K/min). The phase formation of the materials was evaluated using X-ray diffraction (XRD) with Cu-K α radiation (Bruker AXS, Karlsruhe, Germany, Advance D8). Rietveld refinements were performed using the software Topas version 6 (Bruker AXS). The particle size of the powders was measured using laser diffraction (Malvern Mastersizer 2000, Malvern, UK). The specific surface S of the powders was determined from nitrogen adsorption isotherms (BET, Nova 2000, Quantachrome Instruments, Boynton Beach, FL, USA); a mean particle size d_{BET} was estimated using the relation $d_{\text{BET}} = 6/\rho \cdot S$ (with density ρ ; assuming spherical particles). Shrinkage measurements were made with a Netzsch DIL402 (Netzsch, Selb, Germany) dilatometer on cylindrical compacts during heating to 1000 °C with a 5 K/min heating rate. The bulk density of sintered samples was determined using Archimedes' method with heptane as liquid. The microstructure of the samples was studied on polished and thermally etched samples with a scanning electron microscope (SEM, Ultra 55, Zeiss Microscopy GmbH, Jena, Germany). The mean grain size g_{50} was determined using the line intercept method in combination with a factor of 1.57 as proposed by Mendelson [28]. Samples exhibiting exaggerated grain growth were not analyzed using this method and their grain size was generally noted with 1000 μm . Elemental analysis was performed using a Bruker EDX system on polished and non-etched samples. The permeability of sintered toroids was measured using an Agilent E4991A (St. Clara, CA, USA) impedance/materials analyzer.

5. Conclusions

The phase formation, microstructure, and permeability of Fe-deficient Ni-Cu-Zn ferrites $\text{Ni}_{0.30}\text{Cu}_{0.20}\text{Zn}_{0.50+z}\text{Fe}_{2-z}\text{O}_{4-(z/2)}$ ($0 \leq z \leq 0.06$) were investigated as a function of sintering temperature T_s . It is shown that, compared with stoichiometric ferrites ($z = 0$), Fe-deficient ferrites exhibit specific shrinkage behavior, microstructure, and permeability:

1. With increasing Fe-deficiency z , the temperature of the maximum shrinkage rate is shifted from $T = 1000$ °C for $z = 0$ towards $T < 900$ °C for $z = 0.02$. Firing at 900 °C gives dense samples for Fe-deficient ferrites ($z > 0$) only.

2. Stoichiometric ferrites exhibit regular grain growth until, at 1150 °C, exaggerated grain growth sets in owing to the formation of a Cu-oxide liquid phase.
3. Fe-deficient ferrites consist of ferrite grains and a CuO second phase distributed at the triple points. At sintering temperatures of about $T_s > 1050$ °C, CuO is reduced to Cu₂O and the formation of a eutectic triggers exaggerated ferrite grain growth. These ferrites with large grains exhibit reduced permeability because (i) non-magnetic pores and Cu oxide grain boundary phases reduce the saturation magnetization and permeability and (ii) pores within ferrite grains and the grain boundary phase act as pinning centers for domain walls, and thus also reduce the permeability.
4. The formation of intra-crystalline porosity sets in already at intermediate sintering temperatures in regularly grown ferrite grains, leading to a reduction in permeability.
5. Sintering protocols of Fe-deficient Ni-Cu-Zn ferrites require optimization of a delicate balance of inter- and intra-crystalline porosity on one hand, and concentration and chemistry of Cu oxide second phases at triple points and grain boundaries on the other hand, to tailor a maximum permeability performance.

Author Contributions: Conceptualization, C.P. and J.T.; methodology, C.P.; investigation, C.P.; writing—original draft preparation, C.P.; writing—review and editing, J.T.; supervision, J.T.; project administration, J.T.; funding acquisition, J.T. All authors have read and agreed to the published version of the manuscript.

Funding: This work was funded by the Deutsche Forschungsgemeinschaft DFG (Germany) with grant To 165/9-1.

Institutional Review Board Statement: Not applicable.

Informed Consent Statement: Not applicable.

Data Availability Statement: Not applicable.

Conflicts of Interest: The authors declare no conflict of interest.

References

1. Goldman, A. *Handbook of Modern Ferromagnetic Materials*, 1st ed.; Kluwer Academic Publishers: Boston, MA, USA; Dordrecht, The Netherlands; London, UK, 1999.
2. Nomura, T.; Nakano, A. New evolution of ferrite for multilayer chip components. In Proceedings of the Sixth International Conference on Ferrites, Tokyo, Japan, 29 September–2 October 1992; pp. 1198–1201.
3. Nakano, A.; Nomura, T. Multilayer Chip Inductors. *Ceram. Trans. A Cer.* **1999**, *97*, 285–304.
4. Hsiang, H.I. Progress in materials and processes of multilayer power inductors. *J. Mater. Sci. Mater. Electron.* **2020**, *31*, 16089–16110. [[CrossRef](#)]
5. Mürbe, J.; Töpfer, J. Ni-Cu-Zn Ferrites for low temperature firing: II. Effects of powder morphology and Bi₂O₃ addition on microstructure and permeability. *J. Electroceramics* **2006**, *16*, 199–205. [[CrossRef](#)]
6. Hsiang, H.I.; Chueh, J.F. Bi₂O₃ addition effects on the sintering mechanisms, magnetic properties and DC superposition behavior of NiCuZn ferrites. *Int. J. Appl. Ceram. Technol.* **2015**, *12*, 1008–1015. [[CrossRef](#)]
7. Su, H.; Zhao, C. Correlation between microstructure and permeability stability of ferrite materials. *Ceram. Int.* **2018**, *44*, 2304–2310. [[CrossRef](#)]
8. Wang, Y.; Jing, Y. Comparison of magnetic properties of low-temperature fired NiCuZn ferrites under low- and high-Bi₂O₃ doping modes. *J. Electron. Mater.* **2020**, *49*, 3325–3331. [[CrossRef](#)]
9. Low, K.O.; Sale, F.R. The development and analysis of property-composition diagrams on gel-derived stoichiometric NiCuZn ferrite. *J. Magn. Magn. Mater.* **2003**, *256*, 221–226. [[CrossRef](#)]
10. Mürbe, J.; Töpfer, J. Ni-Cu-Zn Ferrites for low temperature firing: I. Ferrite compositions and its effects on sintering behavior and permeability. *J. Electroceramics* **2005**, *15*, 215–221. [[CrossRef](#)]
11. Zhiyuan, L.; Maoren, X. Effects on iron deficiency on magnetic properties of (Ni_{0.76}Zn_{0.24})O(Fe₂O₃)_{0.575} ferrite. *J. Magn. Magn. Mater.* **2000**, *219*, 9–14. [[CrossRef](#)]
12. Su, H.; Zhang, H. Effects of composition and sintering temperature on properties of NiZn and NiCuZn ferrites. *J. Magn. Magn. Mater.* **2007**, *310*, 17–21. [[CrossRef](#)]
13. Su, H.; Tang, X. Influence of Fe-deficiency on electromagnetic properties of low-temperature fired NiCuZn ferrites. *J. Magn. Magn. Mater.* **2010**, *322*, 1779–1783. [[CrossRef](#)]
14. Mürbe, J.; Töpfer, J. Low temperature sintering of sub-stoichiometric Ni-Cu-Zn ferrites: Shrinkage, microstructure and permeability. *J. Magn. Magn. Mater.* **2012**, *324*, 578–583. [[CrossRef](#)]

15. Hsiang, H.I.; Wu, J.L. Copper-rich phase segregation effects on the magnetic properties and DC-bias-superpositions characteristics of NiCuZn ferrites. *J. Magn. Magn. Mater.* **2015**, *374*, 367–371. [[CrossRef](#)]
16. Sakellari, D.; Tsakaloudi, V. Microstructural phenomena controlling losses in NiCuZn ferrites as studied by transmission electron microscopy. *J. Am. Soc.* **2008**, *91*, 366–371. [[CrossRef](#)]
17. Sun, K.; Lan, Z. Phase formation, grain growth and magnetic properties of NiCuZn ferrites. *J. Magn. Magn. Mater.* **2011**, *323*, 927–932. [[CrossRef](#)]
18. Barba, A.; Clausell, C. ZnO and CuO crystal precipitation in sintering Cu-doped Ni-Zn ferrites. I. Influence of dry relative density and cooling rate. *Eur. Ceram. Soc.* **2011**, *31*, 2119–2128. [[CrossRef](#)]
19. Barba, A.; Clausell, C. ZnO and CuO crystal precipitation in sintering Cu-doped Ni-Zn ferrites. II. Influence of sintering temperature and sintering time. *Eur. Ceram. Soc.* **2017**, *37*, 169–177. [[CrossRef](#)]
20. Nazrin, S.; Sharmin, M. Fabrication and unravelling the impact of iron-deficiency amount on crystal structure, micromorphology, elastic and electromagnetic properties of $\text{Ni}_{0.25}\text{Cu}_{0.13}\text{Zn}_{0.62}\text{Fe}_{2-x}\text{O}_{4-3x/2}$ ferrites under different sintering conditions. *J. Mater. Sci. Mater. Electron.* **2021**, *32*, 4592–4628. [[CrossRef](#)]
21. Li, Y.; Xu, M. Structural and room-temperature ferromagnetic properties of Fe-doped CuO nanocrystals. *J. Appl. Phys.* **2010**, *107*, 113908. [[CrossRef](#)]
22. Nasir, M.; Patra, N. X-ray structural studies on solubility of Fe substituted CuO. *RSC Adv.* **2016**, *6*, 103571. [[CrossRef](#)]
23. Smit, J.; Wijn, J. *Ferrite*; Philips Technische Bibliotheek: Eindhoven, The Netherlands, 1962.
24. Roberts, H.S.; Hastings Smith, F. The System Copper: Cupric Oxide: Oxygen. *J. Am. Chem. Soc.* **1921**, *43*, 1061–1079. [[CrossRef](#)]
25. Su, H.; Zhang, H. Effects of microstructure on permeability and power loss characteristics of the NiZn ferrites. *J. Magn. Magn. Mater.* **2008**, *320*, 483–485. [[CrossRef](#)]
26. Su, H.; Zhang, H. Influence of microstructure on permeability dispersion and power loss of NiZn ferrite. *J. Appl. Phys.* **2008**, *103*, 483–485. [[CrossRef](#)]
27. Johnson, M.T.; Visser, E.G. A coherent model for the complex permeability in polycrystalline ferrites. *IEEE Trans. Magn.* **1990**, *26*, 1987–1989. [[CrossRef](#)]
28. Mendelson, M.L. Average grain size in polycrystalline ceramics. *J. Am. Ceram. Soc.* **1969**, *52*, 443–446. [[CrossRef](#)]